Journal of Solid State Chemistry 183 (2010) 1823–1828

Contents lists available at ScienceDirect

Journal of Solid State Chemistry

journal homepage: www.elsevier.com/locate/jssc

The local structure and composition of $Ba_4Nb_2O_9$-based oxycarbonates

Jana Bezjak [a,*], Artem M. Abakumov [b], Aleksander Rečnik [c], Marjeta Maček Kržmanc [a], Boštjan Jančar [a], Danilo Suvorov [a]

[a] Advanced Materials Department, Jožef Stefan Institute, Jamova cesta 39, SI-1000 Ljubljana, Slovenia
[b] EMAT, University of Antwerp, Groenenborgerlaan 171, B-2020 Antwerp, Belgium
[c] Nanostructured Materials Department, Jožef Stefan Institute, Jamova cesta 39, SI-1000 Ljubljana, Slovenia

ARTICLE INFO

Article history:
Received 23 March 2010
Received in revised form
4 June 2010
Accepted 8 June 2010
Available online 12 June 2010

Keywords:
Oxycarbonate
2H-hexagonal perovskite derivatives
Incommensurately modulated composite structure
Nanoscale twinning
One-dimensional disorder

ABSTRACT

X-ray powder-diffraction (XRD), high-resolution transmission electron microscopy (HRTEM), electron diffraction (ED), infrared spectroscopy (IR), thermogravimetry (TG) and mass spectroscopy (MS) were performed to investigate the composition and the crystal structure of tetra-barium di-niobate (V) $Ba_4Nb_2O_9$. The TG, MS and IR studies revealed that the compound is a hydrated oxycarbonate. Assuming that the carbonate stoichiometrically replaces oxygen, the composition of the low-temperature α-modification, obtained by slow cooling from 1100 °C, corresponds to $Ba_4Nb_2O_{8.8}(CO_3)_{0.2}\cdot 0.1H_2O$, while the quenched high-temperature γ-modification has the $Ba_4Nb_2O_{8.42}(CO_3)_{0.58}\cdot 0.38H_2O$ composition. The α-phase has a composite incommensurately modulated structure consisting of two mutually interacting $[Ba]_\infty$ and the $[(Nb,\square)O_3]_\infty$ subsystems. The composite modulated crystal structure of the α-phase can be described with the lattice parameters $a=10.2688(1)$ Å, $c=2.82426(8)$ Å, $\mathbf{q}=0.66774(2)\mathbf{c}^*$ and a superspace group $R\bar{3}m(00\gamma)0s$. The HRTEM analysis demonstrates the nanoscale twinning of the trigonal domains parallel to the {1 0 0} crystallographic planes. The twinning introduces a one-dimensional disorder into the $[(Nb,\square)O_3]_\infty$ subsystem, which results in an average $P\bar{6}2c$ crystal structure of the α-phase. Possible places for the carbonate group in the structure are discussed using a comparison with other hexagonal perovskite-based oxycarbonates.

1. Introduction

A recent investigation of the phase transitions in $Ba_4Nb_2O_9$ revealed that this compound demonstrates an extremely complex relationship between the different polymorphs and their hydrated forms [1–3]. According to the findings of Ling et al. [3], the γ-I $Ba_4Nb_2O_9$ phase is stable above 1370 K. This form can be quenched below 1210–950 K, and then with further cooling it takes up water, forming hydrates with the compositions $Ba_4Nb_2O_9\cdot\frac{1}{6}H_2O$ (the γ-II phase) and $Ba_4Nb_2O_9\cdot\frac{1}{3}H_2O$ (the γ-III phase). The γ-I and γ-II phases crystallize in an orthorhombic unit cell with different superstructures. The γ-III phase has the same subcell, but it is monoclinically distorted. When the γ-I phase is slowly cooled below 1370–1210 K, it transforms into a hexagonal α phase, which also takes up water to the $Ba_4Nb_2O_9\cdot\frac{1}{6}H_2O$ composition after being cooled down to 370 K. The unit cell parameters and the crystal structure of α-$Ba_4Nb_2O_9$ demonstrate that this compound belongs to the family of hexagonal perovskites $A_{1+x}(A'_xB_{1-x})O_3$, based on the 2H close-packed structure. The hexagonal close-packing in such compounds consists of the A_3O_9 and anion-deficient $A_3A'O_6$ layers [4,5]. The B cations are located in the octahedral cavities between the close-packed layers, whereas the A′ cations occupy the trigonal-prismatic sites. The octahedra and trigonal prisms share faces and form columns running along the hexagonal *c*-axis. The crystal structure of these compounds cannot be simply described in terms of mixed layer sequences, but must be considered as a composite structure, consisting of two mutually modulated subsystems [6]. The first subsystem $[(B,A')O_3]_\infty$ forms a hexagonal lattice of columns composed of trigonal-prismatic and octahedral units alternating along the *c*-axis of the hexagonal unit cell, while the other subsystem, i.e., $[A]_\infty$, consists of chains formed by A-cations. The two subsystems have common unit cell dimensions within the *ab* plane, but different periodicities along the *c*-axis, i.e., c_1 and c_2, giving rise to a modulation vector $\mathbf{q}=\gamma\mathbf{c}_1^*$ with $\gamma=c_1/c_2$, related to the *x* in the chemical formula $\gamma=(1+x)/2$. Alternatively, the chemical composition can be described with the general formula $A_{3n+3m}A'_nB_{3m+n}O_{9\,m+6n}$ $(x=n/(3m+2n))$, where n/m is the ratio between the numbers of the A_3O_9 and $A_3A'O_6$ layers [6]. Based on this formalism the α-$Ba_4Nb_2O_9$ structure belongs to the $n=3$, $m=1$ member, taking into account that the A′ position in this structure is taken by a cation vacancy. The crystal structures of the $A_{3n+3m}A'_nB_{3m+n}O_{9m+6n}$ compounds can be described with the unified superspace model in the frame of the $R\bar{3}$ $m(00\gamma)0s$ (3+1)-dimensional space group. The superspace symmetry allows a derivation of all the possible 3-dimensional space groups for the

* Corresponding author. Fax: +386 1 4773 875.
E-mail addresses: jana.bezjak@ijs.si, jana.bezjak@gorenje.si (J. Bezjak).

0022-4596/$ - see front matter © 2010 Elsevier Inc. All rights reserved.
doi:10.1016/j.jssc.2010.06.003

commensurately modulated cases, i.e., when the ratio between the c-parameters of the subsystems $\gamma = c_1/c_2$ is a rational number (or can be approximated by a rational number with a reasonably small denominator). According to the structure reported by Ling et al. [3], α-$Ba_4Nb_2O_9$ corresponds to a commensurate case with $\gamma = 2/3$. However, the space group $P\bar{6}2c$, proposed for α-$Ba_4Nb_2O_9$ by Ling et al., cannot be derived from the $R\bar{3}m(00\gamma)0s$ (3+1)-dimensional space group. This inspired us to investigate in more detail the local structure of α-$Ba_4Nb_2O_9$ in order to resolve this discrepancy. In this contribution we propose a local structure model for this compound and we demonstrate that both the γ-$Ba_4Nb_2O_9$ and α-$Ba_4Nb_2O_9$ phases are not hydrate as suggested by Ling et al. [3], but the hydrated oxycarbonates $Ba_4Nb_2O_{8.42}(CO_3)_{0.58} \cdot 0.38H_2O$ and $Ba_4Nb_2O_{8.8}(CO_3)_{0.2} \cdot 0.1H_2O$. This result is not surprising taking into account many known perovskite-based oxycarbonates, especially with high content of alkali-earth metal cations [7–11].

2. Experimental

A polycrystalline sample with the nominal $Ba_4Nb_2O_9$ composition was prepared with a solid-state reaction from stoichiometric quantities of $BaCO_3$ and Nb_2O_5 powders (99.8%, Alfa Aesar, Karlsruhe, Germany). The mixture was first ball-milled in a planetary mill for 2 h using yttria-stabilized zirconia balls and pure ethanol as a mixing media. After drying, the powder was calcined at 800 °C in air for 20 h, then ground, and re-calcined at 900 and 1000 °C for 20 h [1,2]. The calcined and milled powders were uniaxially pressed into 10-mm pellets. Green bodies were then fired on a sacrificial pellet of the same composition in an alumina crucible at 1300 °C in the ambient air. The final thermal treatment was performed in two different ways: sample I was heated at 1100 °C for 5 h and slowly cooled (corresponding to the conditions of the γ-I→α-$Ba_4Nb_2O_9$ transition according to Ling et al. [3]); sample II was heated at 1300 °C for 48 h and quenched (corresponding to the conditions of the γ-I→γ-II $Ba_4Nb_2O_9$ transition according to Ling et al. [3]).

The progress of the solid-state reactions after each calcination step was monitored with X-ray powder diffraction (XRD) using a Panalytical X'Pert PRO MPD X-ray diffractometer with Cu$K\alpha 1$ radiation ($\lambda = 1.5406$ Å). The treatment of the XRD patterns was performed with the JANA2000 program [12].

For the TEM observations the samples were cut into 3-mm discs, which were mechanically polished to a thickness of ~100 μm and dimpled (Dimple Grinder, Gatan) to ~20 μm in the disk center. The TEM specimens were produced by ion-milling (RES 010, Bal-Tec) with 4-keV Ar^+ ions at an incidence angle of 10° until perforation of the central disk area occurred. Prior to the TEM work the samples were coated with a 4-nm thin film of amorphous carbon to improve the conductivity. Electron diffraction (ED) studies were performed using a Jeol JEM-2010 TEM, while the high-resolution TEM studies were performed using a 200-kV FEG-TEM Jeol JEM-2010 F. For simulating the HRTEM images a multi-slice method from the EMS program code was used [13].

Differential thermal (DTA) and thermo-gravimetric (TG) analyses were studied on a Netzsch Jupiter 449 simultaneous thermal analysis instrument coupled with a Netzsch QMS 403C Aëolos quadrupole mass spectrometer. The analysis was performed in air from 25° to 1000 °C with heating and cooling rates of 10 °C/min using an Al_2O_3 crucible with a lid.

Infrared spectra were collected with a Bruker spectrometer IFS 66/S using standard KBr technique.

3. Results

3.1. Thermal analysis and FT-IR spectroscopy: the composition of γ- and α-forms of $Ba_4Nb_2O_9$

Ling et al. [3] reported that both the γ-$Ba_4Nb_2O_9$ (sample II) and the α-$Ba_4Nb_2O_9$ (sample I) undergo several dehydration steps when heated from room temperature to 900 °C. In order to verify whether γ-$Ba_4Nb_2O_9$ and α-$Ba_4Nb_2O_9$ eventually take up water, the TG analysis combined with mass spectrometry (MS) of the evolved gases was performed. For γ-$Ba_4Nb_2O_9$ the TG analysis (Fig. 1) revealed the same weight-loss curve as reported by Ling et al. [3]: the process occurs in four stages, starting at ~80, 225, 525 and 800 °C (Fig. 1a). Surprisingly, only the first stage corresponds to a water loss, whereas the three subsequent steps correspond to the loss of CO_2, i.e., to the decarbonization. The temperatures of last two decarbonization steps coincide well with the onsets of the γ-III→γ-II and γ-II→γ-I structural transitions. This clearly indicates that CO_2 evolves from the γ-$Ba_4Nb_2O_9$ structure and not from an extrinsic admixture. A similar TG curve with a single dehydration step at ~100 °C and three decarbonization steps at 450, 525 and 750 °C were observed for the α-$Ba_4Nb_2O_9$ phase (Fig. 1b). The overall content of the carbonate groups and water was estimated from the weight losses at every decarbonization and dehydration step on the TG curves, assuming that the Nb^{5+} cations do not change their valent

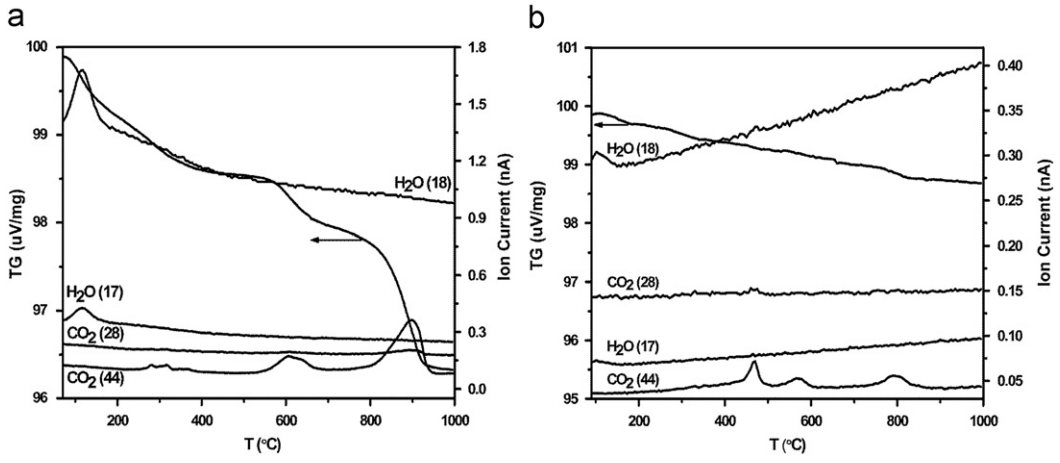

Fig. 1. The TG and MS curves for the "γ-$Ba_4Nb_2O_9$" and "α-$Ba_4Nb_2O_9$" phases. The evolution of H_2O and CO_2 was monitored by m/z fragments of 18, 17 and m/z fragments of 44, 28, respectively.

state. Thus, the compositions of the γ-$Ba_4Nb_2O_9$ and α-$Ba_4Nb_2O_9$ phases can be assessed as $Ba_4Nb_2O_{8.42}(CO_3)_{0.58}\cdot 0.38H_2O$ and $Ba_4Nb_2O_{8.8}(CO_3)_{0.2}\cdot 0.1H_2O$, respectively. According to the standard deviation in the measured weight for the TG equipment used, the errors in the CO_2 and H_2O content do not exceed ~0.05%.

The presence of the carbonate groups was additionally confirmed by FT-IR analyses (Fig. 2). The IR spectra of the $Ba_4Nb_2O_{8.42}(CO_3)_{0.58}\cdot 0.38H_2O$ and $Ba_4Nb_2O_{8.8}(CO_3)_{0.2}\cdot 0.1H_2O$ show the typical absorption bands, i.e., at 858 and 1425 cm^{-1}, corresponding to the of CO_3^{2-} anion [14]. The peak located at 858 cm^{-1} matches the out-of-plane bending modes of the CO_3^{2-} group, while that at ~1425 cm^{-1} belongs to the asymmetric stretching vibrations of the carbonate anion. The higher intensity of both bands in the IR spectrum of the $Ba_4Nb_2O_{8.42}(CO_3)_{0.58}\cdot 0.38H_2O$ compared to those in the IR spectrum of the $Ba_4Nb_2O_{8.8}(CO_3)_{0.2}\cdot 0.1H_2O$ agrees with the higher mass loss due to CO_2 removal. The two peaks with their centers at ~447 and ~518 cm^{-1} correspond to the O–Nb–O bending vibrations, while the bands at 609–721 cm^{-1} correspond predominantly to the internal stretching of the NbO_6 octahedra [15]. Additionally, the IR spectra of the powders show a broad, high-frequency band at ~3400 cm^{-1} that corresponds to the symmetric and asymmetric stretching vibrations of surface-adsorbed hydroxyl groups (Ba–OH^-) or to the O–H stretching of physically bounded H_2O. Moreover, a very weak peak at 1650 cm^{-1} belongs to the H–O–H bending of water.

3.2. Lattice parameters and symmetry of $Ba_4Nb_2O_{8.8}(CO_3)_{0.2}\cdot 0.1H_2O$

The ED patterns of $Ba_4Nb_2O_{8.8}(CO_3)_{0.2}\cdot 0.1H_2O$ (sample I), were indexed as a composite modulated structure with the diffraction vector $\mathbf{H}=h\mathbf{a}^*+k\mathbf{b}^*+l\mathbf{c}_1^*+m\mathbf{q}$, $\mathbf{q}=\gamma\mathbf{c}_1^*=(1/\gamma)\mathbf{c}_2^*$, where a, b, c_1 and c_2 ($a=b\approx 10.25$ Å, $c_1\approx 2.83$ Å, $c_2\approx 4.23$ Å) are the lattice parameters of the hexagonal unit cells of the $[(Nb,\square)O_3]_\infty$ and $[Ba]_\infty$ subsystems, respectively (□—cation vacancy) (Fig. 3). Due to small content of the carbonate groups and water we will not take their presence into account for the structure analysis for clarity.

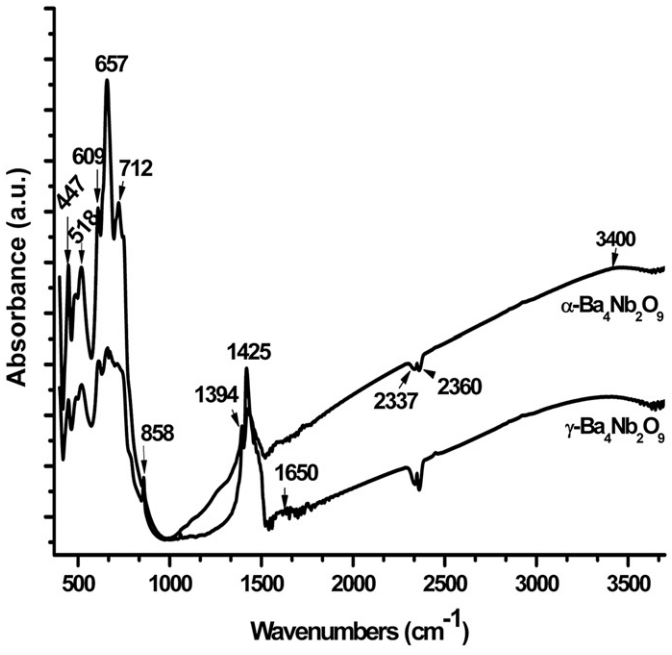

Fig. 2. Infrared spectra of the $Ba_4Nb_2O_{8.42}(CO_3)_{0.58}\cdot 0.38H_2O$ (a) and $Ba_4Nb_2O_{8.8}(CO_3)_{0.2}\cdot 0.1H_2O$ phases (b).

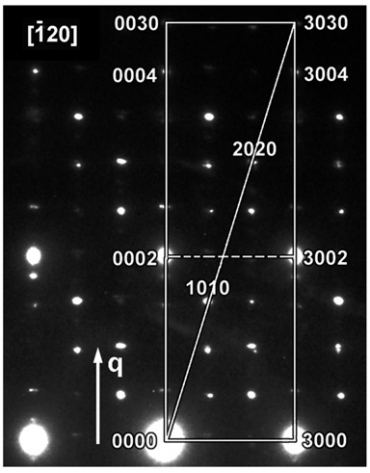

Fig. 3. The [1̄20] ED pattern of $Ba_4Nb_2O_{8.8}(CO_3)_{0.2}\cdot 0.1H_2O$. The reciprocal unit cell of the $[(Nb,\square)O_3]_\infty$ (*hkl*0 reflections) and $[Ba]_\infty$ (*hk*0*m* reflections) subsystems are marked. The $\mathbf{q}=\gamma\mathbf{c}_1^*=(1/\gamma)\mathbf{c}_2^*$ modulation vector is indicated by an arrow.

The reflections on the ED patterns of $Ba_4Nb_2O_{8.8}(CO_3)_{0.2}\cdot 0.1H_2O$ can be divided into four groups: the *hkl*0 reflections belong to the $[(Nb,\square)O_3]_\infty$ subsystem, the *hk*0*m* reflections originate from the $[Ba]_\infty$ subsystem, the *hk*00 reflections are common to both subsystems, and the *hklm* reflections are satellites arising from the mutual modulation of the subsystems. The positions of the satellite reflections on the [1̄20] ED pattern (Fig. 3) roughly corresponds to $\gamma=\frac{2}{3}$. However, a displacement of the satellites along $\mathbf{c}^*$ from their commensurate positions is obvious, indicating that the $Ba_4Nb_2O_{8.8}(CO_3)_{0.2}\cdot 0.1H_2O$ structure is in fact incommensurately modulated, with the γ-component of the modulation vector deviating slightly from $\frac{2}{3}$. The reflection conditions, observed from the ED patterns, are in agreement with the superspace group $R\bar{3}m(00\gamma)0s$. Some of the satellites, forbidden by the m_s plane, are visible on the ED patterns due to multiple diffraction and do not violate the reflection conditions [16]. A similar method of indexation can be applied to the powder XRD pattern of $Ba_4Nb_2O_{8.8}(CO_3)_{0.2}\cdot 0.1H_2O$. The lattice parameters and the γ component of the modulation vector were refined using a LeBail fit: $a=10.2688(1)$ Å, $c_1=2.82426(8)$ Å, $\gamma=0.66774(2)$ (Fig. 4). A remarkable feature of the XRD pattern is a strong broadening of the reflections belonging to the $[(Nb,\square)O_3]_\infty$ subsystem, which was taken into account using a method described by Stephens [17]. At the same time, the common *hk*00 reflections and the reflections from the $[Ba]_\infty$ subsystem remain sharp. This indicates the one-dimensional disorder of the $[(Nb,\square)O_3]_\infty$ subsystem, which might be related to the substitution of vacant cations sites by carbonate groups.

Assuming the closest commensurate value of $\gamma=\frac{2}{3}$, the possible 3D symmetries for α-$Ba_4Nb_2O_9$ can be derived as $P\bar{3}$, $P321$ and $P3$. These space groups are different from the $P\bar{6}2c$ space group suggested by Ling et al. [3]. The analysis of the "ideal" symmetry (i.e., taking into account both the positions and the intensities of the reflections) of the [1̄20] ED pattern of $Ba_4Nb_2O_{8.8}(CO_3)_{0.2}\cdot 0.1H_2O$ sheds light on the true symmetry of this compound (Fig. 5) [18]. For the $P\bar{6}\ 2c$ space group, corresponding to the 6-2*m* crystallographic point group, the point symmetry of the [1̄20] ED pattern should be 2*mm* (Fig. 5c), but the experimental ED pattern clearly demonstrates the absence of the mirror planes and the presence of only the twofold axis (Fig. 5a). This is in agreement with the crystallographic point group 321 and leaves the $P321$ space group as the only choice for the $Ba_4Nb_2O_{8.8}(CO_3)_{0.2}\cdot 0.1H_2O$ structure (Fig. 5b). We believe that the explanation for the discrepancy in the space

symmetries determined from ED and the neutron powder-diffraction data originates from the defect structure of $Ba_4Nb_2O_{8.8}(CO_3)_{0.2}\cdot 0.1H_2O$, which was investigated using HRTEM.

3.3. HRTEM analysis of the local structure of $Ba_4Nb_2O_{8.8}(CO_3)_{0.2}\cdot 0.1H_2O$

The HRTEM images along the [$\bar{1}$20] direction revealed multiple mirror twins with the {1 0 0} crystallographic planes as twin planes. Two domains separated by a vertical twin boundary are shown in Fig. 6. The domains on the left- and right-hand sides of the twin boundary clearly demonstrate the absence of the mirror planes, in agreement with the point group 321. The [$\bar{1}$20] HRTEM image recorded from a single domain is shown in Fig. 7. A crystal thickness of 5 nm was estimated from the distance (d) of the imaged area to the edge of the crystal foil and the ion-milling angle (α) from the trigonometric relation $t=d\tan(\alpha)$, whereas the defocus value was estimated by matching the intensity profile of the Fourier transform from the amorphous edge and the simulated contrast transfer functions (CTFs) computed for the experimental imaging conditions. The best match was found at a focus of about $f=\sim 99$ nm, where the lattice image is characterized by a square pattern of strong white dots residing at the corners of the unit cell. According to the theoretical images, these dots are at the positions of the cation vacancies in the $[(Nb,\square)O_3]_\infty$ subsystem. The regular arrangement of these dots reflects the perfect local order within a single domain. The distance between the arrays of dots along the c-axis is $\sim$2.1 Å, which corresponds to the distance between the close-packed layers. For a calculation of the theoretical images of the $P\bar{6}2c$ model the $Sr_4Ru_2O_9$ structure [19] was used and modified after Ling et al.[3], including the suggested partial occupancies for niobium and oxygen, whereas the $P321$ model was based on the $Sr_4Ni_3O_9$ structure [20]. However, only the $P321$ model successfully reproduces the contrast features of the experimental HRTEM image. A remarkable difference between the two models can be observed in the intensity variations of the

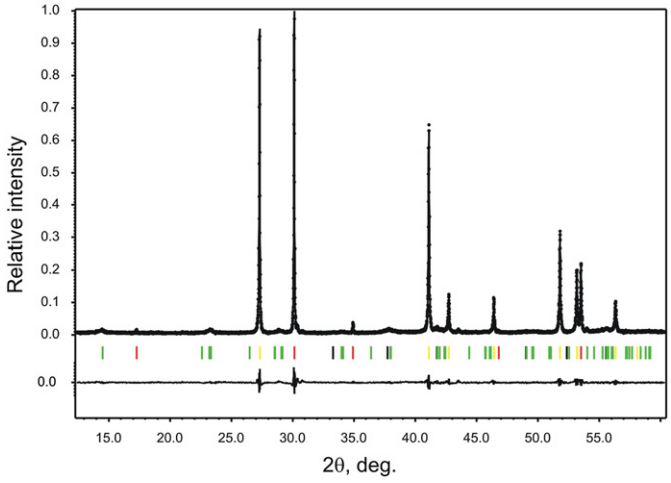

Fig. 4. LeBail fit of the powder XRD pattern of $Ba_4Nb_2O_{8.8}(CO_3)_{0.2}\cdot 0.1H_2O$. The bars mark the positions of the $hkl0$ reflections from the $[(Nb,\square)O_3]_\infty$ subsystem (black), the $hk0m$ reflections from the $[Ba]_\infty$ subsystem (yellow), the $hk00$ reflections common for both subsystems (red) and the $hklm$ satellites up to the second order (green). (For interpretation of the references to colour in this figure legend, the reader is referred to the web version of this article.)

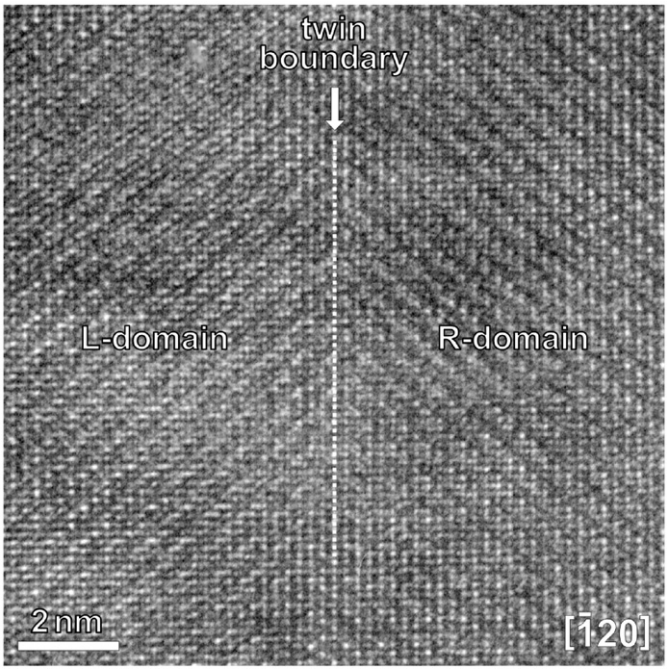

Fig. 6. The [$\bar{1}$20] HRTEM image of $Ba_4Nb_2O_{8.8}(CO_3)_{0.2}\cdot 0.1H_2O$ showing two domains related by a mirror-twin operation.

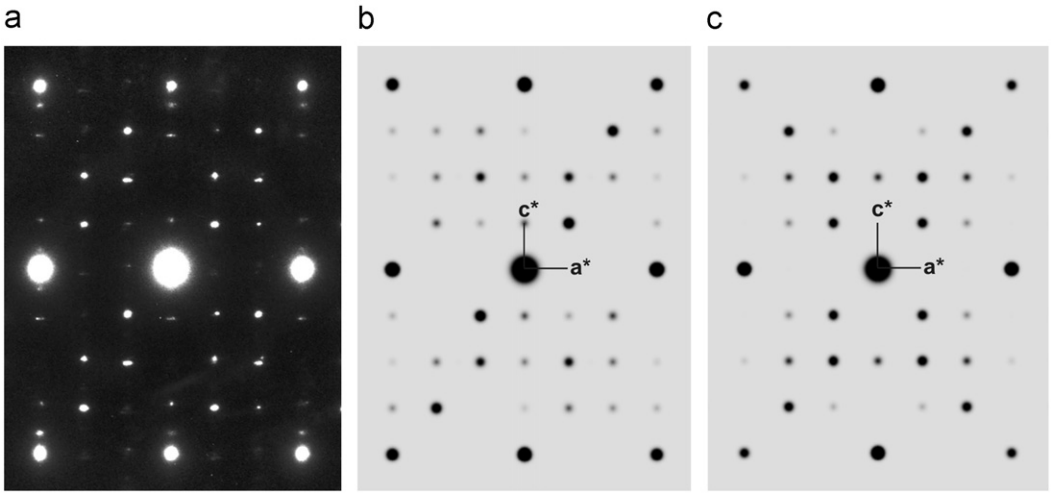

Fig. 5. The [$\bar{1}$20] ED pattern of $Ba_4Nb_2O_{8.8}(CO_3)_{0.2}\cdot 0.1H_2O$ (a) and kinematical ED patterns calculated using the $P321$ (b) and $P\bar{6}$ 2c (c) structure models.

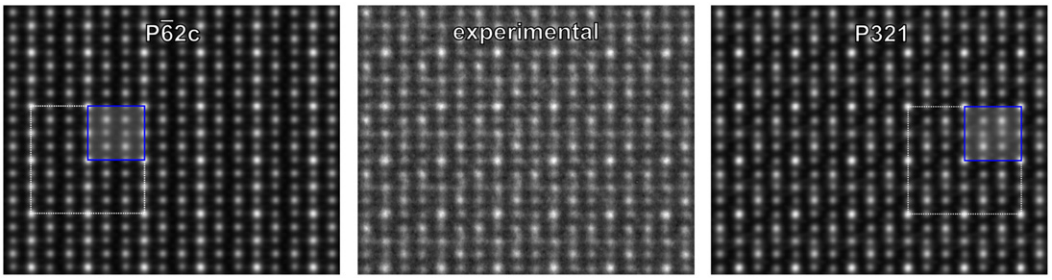

Fig. 7. The experimental [$\bar{1}$20] HRTEM image of $Ba_4Nb_2O_{8.8}(CO_3)_{0.2}\cdot 0.1H_2O$ and the theoretical HRTEM images calculated using the *P*321 and *P*$\bar{6}$ 2*c* structure models. The highlighted squares (image and model) denote the basic repeat unit (unit-cell) of the structure.

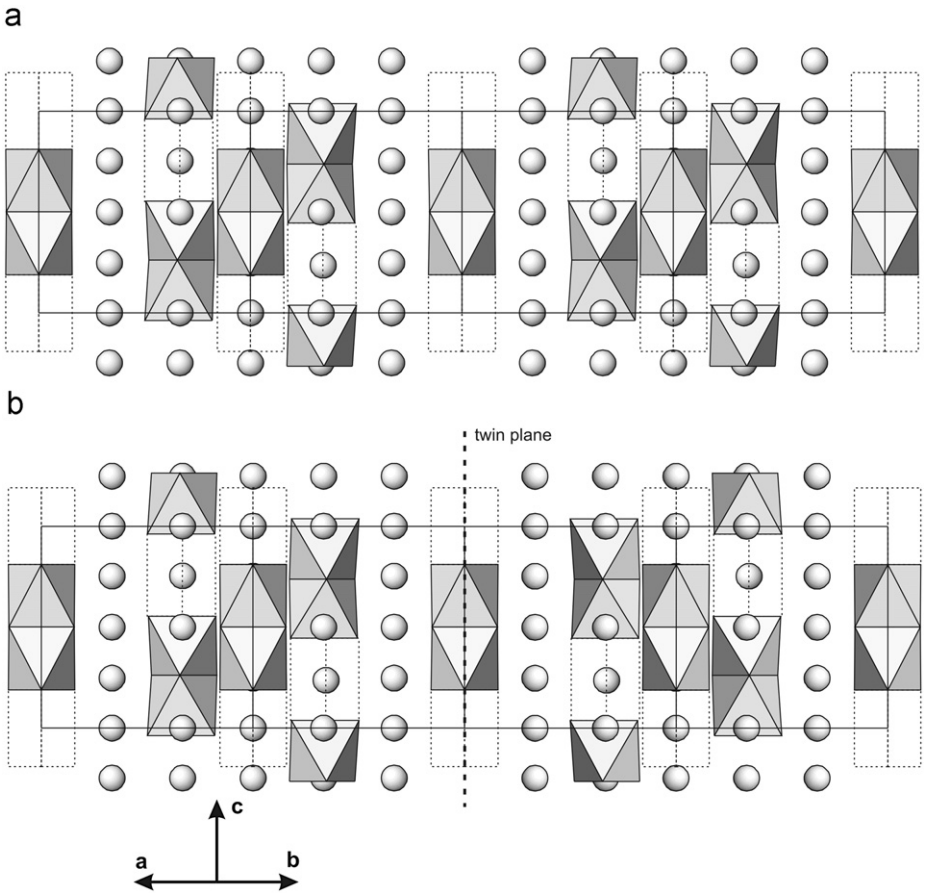

Fig. 8. The *P*321 structure model of $Ba_4Nb_2O_{8.8}(CO_3)_{0.2}\cdot 0.1H_2O$ (a). Two unit cells are shown in the *ab* plane. The Nb atoms are situated in the shaded octahedra, the vacant trigonal prismatic sites are outlined with dashed lines, and the Ba atoms are shown as spheres. The affection of the {1 0 0} twin plane on the *P*321 structure (b). Note that the mirror reflection does not affect the arrangement of the Ba cations, but exchanges the vacant trigonal prisms for the Nb_2O_9 pairs of the face-sharing octahedra and vice versa. A presence of carbonate groups and water is not taken into account in this model.

weaker white dots. Although the *P*321 model correctly replicates the traverse, higher intensity of the neighboring weak dots, as observed in the experimental image, this feature is not reproduced in the simulation based on the *P*$\bar{6}$2*c* model after Ling et al. [3]. To quantify the overall impact of these differences on the image an overall similarity cross-correlation method was used [21]. Quantitative matching of the experimental and the simulated HRTEM images resulted in a cross-correlation coefficient of 0.81 for the *P*$\bar{6}$2*c* model and 0.90 for the *P*321 model, suggesting that the $Sr_4Ni_3O_9$-based model better replicates the basic structural features of the $Ba_4Nb_2O_{8.8}(CO_3)_{0.2}\cdot 0.1H_2O$ rather than the $Sr_4Ru_2O_9$-based model. The main reason for this lies in the fact that this model results from averaged structural neutron powder diffraction data on "α-$Ba_4Nb_2O_9$", i.e. where the *P*321 symmetry was blended by nanoscale twinning of the trigonal domains [3]. In the "α-$Ba_4Nb_2O_9$" crystal structure the Ba atoms demonstrate only a negligible displacement from the {1 0 0} crystallographic planes, which means that these planes are in fact the symmetry elements of the $[Ba]_\infty$ subsystem. Thus, the twinning operation can be considered as a symmetry operation of the $[Ba]_\infty$ subsystem and twinning does not introduce a disorder in the positions of the Ba atoms. In contrast, the {1 0 0} mirror operation is not an intrinsic symmetry operation of the $[(Nb,\square)O_3]_\infty$ subsystem: a mirror reflection applied to the polyhedral chains exchanges the face-sharing NbO_6 octahedra for empty trigonal prismatic sites and vice versa (Fig. 8). The nanoscale {1 0 0} twinning introduces a disorder in the $[(Nb,\square)O_3]_\infty$ subsystem, resulting in the average *P*$\bar{6}$ 2*c* model

observed with the neutron powder diffraction. We cannot derive the location of the carbonate groups and water using the HRTEM images, but the most plausible position is discussed below based on comparison with other known oxycarbonate hexagonal perovskites.

4. Discussion

Thermal analysis and infrared absorption spectroscopy revealed that the compound, generally known as $Ba_4Nb_2O_9$, is actually a hydrated oxycarbonate at room temperature. Most probably, using $BaCO_3$ as an initial material provides a source of the carbonate groups in the final products, even in spite of relatively high annealing temperature of 1300 °C at the final stage of the solid-state reaction. The composition of the low-temperature α-phase corresponds to $Ba_4Nb_2O_{8.8}(CO_3)_{0.2}\cdot 0.1H_2O$, while the quenched high-temperature γ-phase can be described as $Ba_4Nb_2O_{8.42}(CO_3)_{0.58}\cdot 0.38H_2O$. Strong one-dimensional disorder of the $[(Nb,\square)O_3]_\infty$ subsystem affects the powder diffraction data making precise location of the carbonate group questionable even with the use of neutron diffraction data. However, incorporation of the carbonate groups into hexagonal perovskites is not something unusual and assumption can be made on possible place of the carbonate groups in the structure. In the 2H close-packed structure of $Ba_3Co_2O_6(CO_3)_{0.6}$ (which is in fact a parent structure for $Ba_4Nb_2O_{8.8}(CO_3)_{0.2}\cdot 0.1H_2O$ and $Ba_4Nb_2O_{8.42}(CO_3)_{0.58}\cdot 0.38H_2O$), the carbonate groups replace every third chain of the face-sharing CoO_6 octahedra resulting in the carbonate groups to be located nearly at the centers of the Ba triangles in the close-packed layers [22]. This locally reproduces the fragments of the witherite $BaCO_3$ aragonite-type structure [23]. This position seems to be the most plausible place for the carbonate group in the $Ba_4Nb_2O_9$-based oxycarbonates. However, absence of a whole column of the NbO_6 octahedra is not realistic since it would be easily observed on the HRTEM images, as it was demonstrated for $Ba_3Co_2O_6(CO_3)_{0.6}$ [22]. More plausible scenario is a location of the carbonate group at the vacant cation size in the trigonal pyramid between the pairs of the face-sharing NbO_6 octahedra. In this case the carbonate group centers the Ba triangle of the $A_3A'O_6$ layers, occupying a place of the A′ cation. Part of the oxygen atoms from the neighboring NbO_6 octahedra can be eliminated to account for the experimentally observed $Ba_4Nb_2O_{8.8}(CO_3)_{0.2}\cdot 0.1H_2O$ and $Ba_4Nb_2O_{8.42}(CO_3)_{0.58}\cdot 0.38H_2O$ compositions, forming a coordination environment, similar to that observed for the Ru atoms in 6H-$Ba_3(Ru_{1.69}C_{0.31})(Na_{0.95}Ru_{0.05})O_{8.69}$ oxycarbonate [24].

Acknowledgments

This work is based in part on the Ph.D. thesis of Jana Bezjak under Grant no. 3311-04-831835. The financial support by the Slovenian Research Agency under the Programme no.P2 0091 0106 032 entitled "Advanced inorganic materials and technologies" is gratefully acknowledged.

References

[1] J. Bezjak, B. Jančar, A. Rečnik, D. Suvorov, J. Eur. Ceram. Soc. 28 (2008) 2771–2776.
[2] J. Bezjak, A. Rečnik, B. Jančar, Ph. Boullay, I.R. Evans, D. Suvorov, J. Am. Ceram. Soc. 92 (2009) 1806–1812.
[3] Ch.D. Ling, M. Avdeev, R. Kutteh, V.V. Kharton, A.A. Yaremchenko, S. Fialkova, N. Sharma, R.B. Macquart, M. Hoelzel, M. Gutmann, Chem. Mater. 21 (2009) 3853–3864.
[4] C. Dussarrat, Solid State Ionics 108 (1998) 165–173.
[5] R.H. Mitchell, in: Perovskites, modern and ancient, Hexagonal perovskites and related structures, Almaz Press Inc., Ontario, 2007.
[6] J.M. Perez-Mato, M. Zakhour-Nakhi, F. Weill, J. Darriet, J. Mater. Chem. 9 (1999) 2795–2808.
[7] V. Caignaert, B. Domenges, B. Raveau, J. Solid State Chem. 120 (1995) 279–289.
[8] K. Yamaura, Q. Huang, J.W. Lynn, R.W. Erwin, R.J. Cava, J. Solid State Chem. 152 (2000) 374–380.
[9] C. Chaillout, Q. Huang, R.J. Cava, j. Chenavas, A. Santoro, p. Bordet, J.L. Hodeau, J.J. Krajewski, j.p. Levy, M. Marezio, W.F. Peck Jr., Physica C 195 (1992) 335–344.
[10] M. Huve, C. Michel, A. Maignan, M. Hervieu, C. Martin, B. Raveau, Physica C 205 (1993) 219–224.
[11] T.G. Narendra Babu, D.G. Fish, C. Greaves, J. Mater. Chem. 1 (1991) 677–679.
[12] V. Petricek, M. Dusek, and L. Palatinus, (2000). Jana2000. The crystallographic computing system. Institute of Physics, Praha, Czech Republic.
[13] P.A. Staddelmann, Ultramicroscopy 21 (1987) 131–145.
[14] P. Pasierb, S. Komornicki, M. Rokita, M. Rekas, J. Mol. Struct. 596 (2001) 151–156.
[15] G. Wang, X. Han, M. Song, G. Wang, X. Long, Mater. Lett. 60 (2006) 3710–3713.
[16] A.M. Abakumov, A.V. Mironov, V.A. Govorov, M.V. Lobanov, M.G. Rozova, E.V. Antipov, O.I. Lebedev, G.V. Tendeloo, Solid State Sci. 5 (2003) 1117–1125.
[17] P.W. Stephens, J. Appl. Crystallogr. 32 (1999) 281.
[18] J.P. Morniroli, J.W. Steeds, Ultramicroscopy 45 (1992) 219–239.
[19] C. Dussarrat, J. Fompeyrine, J. Darriet, Eur. J. Solid State Inorg. Chem. 32 (1995) 3–14.
[20] F. Abraham, S. Minaud, C. Renard, J. Mater. Chem. 4 (1994) 1763–1764.
[21] Y. Kauffmann, A. Rečnik, W.D. Kaplan, Mater. Char. 54 (2005) 194–205.
[22] K. Boulahya, U. Amador, M. Parras, J.M. Gonzalez-Calbet, Chem. Mater. 12 (2000) 966–972.
[23] J.P.R. de Villiers, Am. Miner 56 (1971) 758–766.
[24] E. Quarez, M. Huvé, F. Abraham, O. Mentré, Solid State Sci. 5 (2003) 951–963.